

1 **Distinct systems serology features in children, elderly and COVID patients**

2
3 Kevin J. Selva^{1*}, Carolien E. van de Sandt^{1,2*}, Melissa M. Lemke^{3*}, Christina Y. Lee^{3*}, Suzanne K.
4 Shoffner^{3*}, Brendon Y. Chua¹, Thi H.O. Nguyen¹, Louise C. Rowntree¹, Luca Hensen¹, Marios
5 Koutsakos¹, Chinn Yi Wong¹, David C. Jackson¹, Katie L. Flanagan^{4,5,6,7}, Jane Crowe⁸, Allen C.
6 Cheng^{9,10}, Denise L. Doolan¹¹, Fatima Amanat^{12,13}, Florian Krammer¹², Keith Chappell¹⁴, Naphak
7 Modhiran¹⁴, Daniel Watterson¹⁴, Paul Young¹⁴, Bruce Wines^{15,16,17}, P. Mark Hogarth^{15,16,17}, Robyn
8 Esterbauer^{1, 18}, Hannah G. Kelly^{1,18}, Hyon-Xhi Tan^{1,18}, Jennifer A. Juno¹, Adam K. Wheatley^{1,18},
9 Stephen J. Kent^{1,18,19}, Kelly B. Arnold³, Katherine Kedzierska^{1*}, Amy W. Chung^{1*}

10

11 * Equally contributed

12 Co-corresponding authors:

13 Amy W Chung

14 Department of Microbiology and Immunology, Peter Doherty Institute for Infection and Immunity,
15 The University of Melbourne, Victoria 3000, Australia

16 awchung@unimelb.edu.au

17

18 Katherine Kedzierska

19 Department of Microbiology and Immunology, Peter Doherty Institute for Infection and Immunity,
20 The University of Melbourne, Victoria 3000, Australia

21 kkedz@unimelb.edu.au

22

23 ¹ Department of Microbiology and Immunology, Peter Doherty Institute for Infection and Immunity,
24 The University of Melbourne, Victoria, Australia

25 ² Department of Hematopoiesis, Sanquin Research and Landsteiner Laboratory, Amsterdam UMC,
26 University of Amsterdam, Amsterdam, Netherlands

27 ³Department of Biomedical Engineering, University of Michigan, Michigan, USA

28 ⁴Department of Infectious Diseases, Launceston General Hospital, Launceston, Tasmania, Australia;

29 ⁵School of Health Sciences, University of Tasmania, Launceston, Tasmania, Australia;

30 ⁶Department of Immunology and Pathology, Monash University, Commercial Road, Melbourne,
31 Victoria, Australia;

32 ⁷School of Health and Biomedical Science, RMIT University, Melbourne, Victoria, Australia.

33 ⁸Deepdene Surgery, Deepdene, Victoria, Australia.

34 ⁹School of Public Health and Preventive Medicine, Monash University, Melbourne, Victoria,
35 Australia.

36 ¹⁰Infection Prevention and Healthcare Epidemiology Unit, Alfred Health, Melbourne, Victoria,
37 Australia.

- 38 ¹¹Centre for Molecular Therapeutics, Australian Institute of Tropical Health & Medicine, James Cook
39 University, Cairns, Queensland, Australia
40 ¹² Department of Microbiology, Icahn School of Medicine at Mount Sinai, New York, New York,
41 USA
42 ¹³Graduate School of Biomedical Sciences, Icahn School of Medicine at Mount Sinai, New York, NY,
43 USA
44 ¹⁴ School of Chemistry and Molecular Bioscience, University of Queensland, Brisbane, Queensland,
45 Australia
46 ¹⁵Immune Therapies Group, Burnet Institute, Melbourne, Victoria, Australia
47 ¹⁶University of Melbourne, Pathology, Vic, Australia
48 ¹⁷Melbourne Sexual Health Centre, Infectious Diseases Department, Alfred Health, Central
49 Clinical School, Monash University, Australia
50 ¹⁸ARC Centre of Excellence in Convergent Bio-Nano Science and Technology, University of
51 Melbourne, Melbourne, Victoria, Australia
52 ¹⁹Melbourne Sexual Health Centre, Infectious Diseases Department, Alfred Health, Central
53 Clinical School, Monash University, Melbourne, Victoria, Australia

54 **Abstract**

55

56 SARS-CoV-2, the pandemic coronavirus that causes COVID-19, has infected millions worldwide,
57 causing unparalleled social and economic disruptions. COVID-19 results in higher pathogenicity and
58 mortality in the elderly compared to children. Examining baseline SARS-CoV-2 cross-reactive
59 coronavirus immunological responses, induced by circulating human coronaviruses, is critical to
60 understand such divergent clinical outcomes. The cross-reactivity of coronavirus antibody responses
61 of healthy children (n=89), adults (n=98), elderly (n=57), and COVID-19 patients (n=19) were
62 analysed by systems serology. While moderate levels of cross-reactive SARS-CoV-2 IgG, IgM, and
63 IgA were detected in healthy individuals, we identified serological signatures associated with SARS-
64 CoV-2 antigen-specific Fcγ receptor binding, which accurately distinguished COVID-19 patients
65 from healthy individuals and suggested that SARS-CoV-2 induces qualitative changes to antibody Fc
66 upon infection, enhancing Fcγ receptor engagement. Vastly different serological signatures were
67 observed between healthy children and elderly, with markedly higher cross-reactive SARS-CoV-2
68 IgA and IgG observed in elderly, whereas children displayed elevated SARS-CoV-2 IgM, including
69 receptor binding domain-specific IgM with higher avidity. These results suggest that less-experienced
70 humoral immunity associated with higher IgM, as observed in children, may have the potential to
71 induce more potent antibodies upon SARS-CoV-2 infection. These key insights will inform COVID-
72 19 vaccination strategies, improved serological diagnostics and therapeutics.

73 **Introduction**

74 Since the first reported coronavirus disease 2019 (COVID-19) patient in December 2019¹, the severe
75 acute respiratory syndrome coronavirus 2 (SARS-CoV-2) has become a global pandemic, infecting
76 millions of individuals worldwide². Though the majority of COVID-19 patients experience mild
77 symptoms, approximately 20% of cases have more severe disease outcomes involving hospitalization
78 or intensive care treatment, especially in those with underlying co-morbidities such as diabetics and
79 cardiovascular disease³. Furthermore, COVID-19 related morbidity and mortality is significantly
80 higher in the elderly population and almost absent in school-aged children⁴. A disproportional
81 outcome in disease severity with increasing age is not unique to the SARS-CoV-2 pandemic, and is
82 observed during previous influenza pandemics⁵. Understanding whether baseline pre-existing
83 immunological responses, induced by previous exposure to seasonal coronaviruses, contributes to
84 such differences may provide important insights to such divergent clinical outcomes between children
85 and elderly.

86

87 Antibodies (Abs) are a vital component of the immune response with demonstrated importance in the
88 control of most viral pathogens. Apart from virus neutralization, Abs have the capacity to engage Fc
89 Receptors (FcRs) or complement to induce Fc effector functions, including Ab-dependent cellular
90 cytotoxicity (ADCC), Ab-dependent cellular phagocytosis (ADCP), or Ab-dependent complement
91 activation (ADCA)⁶. Fc functions are not limited to neutralizing viral epitopes but utilize any
92 available epitope⁶. A previous SARS-CoV (also called SARS-CoV-1) study associated ADCP with
93 viral clearance⁷, where individuals expressing a higher affinity Fc γ RIIa-H131 polymorphism,
94 associated with enhanced Fc functions, had better disease outcomes⁸. However Fc functional Abs may
95 also enhance infection or pathology through Ab-dependent enhancement (ADE), previously observed
96 in some SARS-CoV-1 animal vaccine and *in vitro* studies^{9,10}. Hence, there is an urgent need to
97 understand the Ab responses elicited against SARS-CoV-2, especially given that current COVID-19
98 vaccine strategies are focused upon inducing effective neutralizing Ab responses¹¹, without inducing
99 pathological damage¹².

100

101 **Results**

102 Immature humoral immunity in children

103 In-depth characterization of cross-reactive SARS-CoV-2 Ab responses in healthy children compared
104 to healthy elderly is needed to understand whether pre-existing human coronavirus (hCoV)-mediated
105 Ab immunity potentially contributes to COVID-19 outcome. We designed a cross-reactive CoV
106 multiplex array, including SARS-CoV-2, SARS-CoV-1, MERS-CoV and hCoV (229E, HKU1,
107 NL63) spike (S) and nucleoprotein protein (NP) antigens (**Extended Data Figure 1b**). CoV-antigen-
108 specific levels of isotypes (IgG, IgA, IgM) and subclasses (IgG1, IgG2, IgG3, IgG4, IgA1, IgA2),
109 along with C1q binding (a predictor of ADCA via the classical pathway) and Fc γ RIIa, Fc γ RIIb and

110 Fc γ RIIIa soluble dimer engagement (mimicking Fc γ R immune complex formation associated with the
111 induction of a range of Fc effector functions¹³) were assessed from plasma of 89 children, 98 adults,
112 and 57 elderly individuals (**Extended Data Figure 2a and Extended Data Table 1**), generating a
113 composite dataset of baseline CoV Ab features (14 CoV antigens x 14 detectors = 196 Ab features).

114

115 We compared CoV Ab responses between children and elderly, identifying 58 of 196 (29.6%) Ab
116 features as significantly different, taking into account multiple comparisons (all $p < 0.00037$; **Figure**
117 **1a; Extended Data Table 2**). The volcano plot illustrates the eight Ab features (left) elevated in
118 children, consisting of IgM targeting a range of CoV antigens, including several SARS-CoV-2
119 antigens (S, NP, and the receptor binding domain (RBD), which is involved in binding to host cells
120 and is a key target of neutralizing Abs). Additionally, we observed elevated SARS-CoV-2 Abs that
121 engaged Fc γ RIIa-H131 soluble dimers, associated with increased ADCP responses¹³. Conversely, 50
122 significantly elevated features were observed in the elderly, primarily consisting of IgA and IgG
123 against a range of CoV antigens, along with hCoV-specific Abs that can bind soluble Fc γ RIIIa
124 dimers, associated with increased ADCC^{13,14}.

125

126 Using systems serology¹⁵, we observed vastly different CoV serological signatures between children
127 and elderly (**Figure 1**). Unsupervised multidimensional visualization (Principal Component Analysis;
128 PCA) of all 196 CoV Ab features clearly distinguished children from elderly, with adults spanning
129 these two cohorts although clustering more closely to the elderly (**Figure 1b**). To identify the minimal
130 signatures of Ab features that best distinguished children from elderly, we performed feature selection
131 (Elastic-Net) followed by a supervised multidimensional clustering analysis (Partial Least Squares
132 Discriminant Analysis; PLSDA). Fifteen Ab features selected by Elastic-Net could accurately
133 discriminate between children and elderly (99.1% calibration, 98.6% cross-validation accuracy).
134 Significant separation of PLSDA scores occurred across the first Latent Variable (LV1) ($p < 0.0001$, t
135 = 21.60, LV1-X axis, which accounted for 29.87% of the signature's total variance; **Figure 1c**). The
136 loadings plot of LV1 (**Figure 1d**) confirmed that children have elevated IgM to a range of CoV
137 antigens, and elevated SARS-CoV-2 Abs that engaged Fc γ RIIa-H131 soluble dimers, but also SARS-
138 CoV-1 Abs that engaged Fc γ RIIIa. In comparison, the elderly had elevated IgA, IgG, and Fc γ RIIIa
139 binding Abs to CoV antigens. To better visualize how these Ab features could distinguish children
140 from elderly, we performed unsupervised hierarchical clustering and illustrate that the same
141 serological signatures naturally cluster the majority of children from the elderly (**Figure 1e**). Notably,
142 there were no differences in baseline CoV serological profiles between the sexes (**Figure 1e**), despite
143 males being clinically associated with higher mortality and more severe COVID-19⁴. Correlates of Ab
144 signatures were further confirmed by feature selection followed by multivariate regression analysis
145 (Partial Least Squared Regression; PLSR), including all healthy individuals to analyse correlates
146 across age (**Extended Data Figure 2**).

147

148 To interrogate Ab functionality and cross-reactivity between antigens of selected CoV signatures, we
149 conducted a correlation network analysis, focusing upon significant correlations of Ab features
150 selected by Elastic-Net. The children's network (**Figure 1f**) demonstrates how SARS-CoV-2 Abs that
151 engaged Fc γ RIIa-H131 are associated with SARS-CoV-2 IgG, specifically of IgG1 subclass. SARS-
152 CoV-2 Fc γ RIIa-H131 immune complex formation was also significantly correlated with multiple
153 other SARS-CoV-2 Fc responses, including Fc γ RIIb, C1q, and Fc γ RIIIa. Of interest, SARS-CoV-1
154 Abs that engaged Fc γ RIIIa-V158, were highly correlated with SARS-CoV-2 Ab responses,
155 potentially due to their high sequence similarity (77%) (**Extended Data Figure 3**). A separate highly
156 correlated IgM network of multiple CoV NP antigens was also observed. Collectively, these data
157 suggest that children may have elevated SARS-CoV-2 Abs with the capacity to engage a range of Fc
158 effector functions to SARS-CoV-2 S, in addition to elevated IgM responses to CoV antigens in
159 comparison to elderly. The elderly predominantly had hCoV functional Ab responses to S protein,
160 mediated by IgG1 and elevated IgA1 to SARS-CoV-2 RBD, correlative with IgA1 and IgA2 S and
161 IgA2 RBD responses (**Figure 1g**). Additionally, they had elevated SARS-CoV-2 NP Abs correlating
162 with Fc γ R signatures to a range of CoV. Amino acid (aa) alignment analyses of NP and S1 proteins
163 showed that there is 91% (NP) and 77% (S1) aa similarity between SARS-CoV-2 and SARS-CoV-1
164 proteins, while SARS-CoV-2 and MERS share 47% (NP) aa similarity, hCoVs NL63 and 229E share
165 29% and 26% aa similarity, respectively in NP, and hCoV HKU and 229E share 28% and 27% in S1,
166 respectively (**Extended Data Figure 3c**), supporting the network analyses. Collectively, these data
167 suggest that children have less exposure to CoV antigens but may have enhanced primary humoral
168 immune responses targeted to SARS-CoV-2 compared to elderly.
169

170

HLA-II alleles influence Ab signatures

171 HLA class II allele information was available for a subset of the healthy individuals (children n=84,
172 adults n=17, elderly n=10, **Figure 2; Extended Data Table 1**). To determine whether HLA-II alleles
173 contributed to differences in Ab predisposition, we conducted Elastic-Net and PLSDA to distinguish
174 Ab responses between the two most frequently observed HLA-DQB1, -DRB1 or -DPB1 alleles in our
175 cohort (**Figure 2a, d and g**). Intriguingly, HLA-DQB1*03:01 and HLA-DQB1*06:02 were
176 associated with distinct Ab features (**Figure 2b-c**; calibration 86.4%, and 82.6% cross-validation
177 accuracy), as were HLA-DRB1*07:01 and HLA-DRB1*15:01 (**Figure 2e-f**; calibration 79.1%, and
178 76.3% cross-validation accuracy), along with HLA-DPB1*04:01 and HLA-DPB1*02:01 (82.3%
179 calibration and 72.2% cross-validation accuracy; **Figure 2h-i**). These results suggest that HLA-II
180 allelic repertoires of individuals may affect the development of Ab responses after infection or
181 vaccination, possibly contributing to the variable antigen-specific Ab titers and/or signatures observed
182 across individuals.

183

184 Distinct Fc Ab signature in COVID-19 patients
185 A cohort of 19 SARS-CoV-2 PCR-positive patients (**Extended Data Figure 2a and Extended Data**
186 **Table 3**) were screened for SARS-CoV-2 antigen-specific serological profiles (**Extended Data**
187 **Figure 4**). An individual who was SARS-CoV-2-exposed but remained SARS-CoV-2 PCR-negative,
188 was also assessed (Donor DD1). Elevated SARS-CoV-2-specific Ab responses in COVID-19 patients
189 relative to healthy or the exposed but PCR-negative individual were observed across multiple
190 titrations (**Extended Data Figure 4**). In particular, we found that in the majority of COVID-19
191 patients, the SARS-CoV-2 antigen-specific Abs bound to Fc γ RIIIaV158 and Fc γ RIIaH131 soluble
192 dimers at high levels, even at 1:800 plasma titrations, suggesting potent ADCC and ADCP
193 activity^{13,14,16}.
194
195 Next, we analysed whether COVID-19 patients had distinct serological patterns of SARS-CoV-2
196 antigen-specific Abs of a single isotype (IgG, IgA, or IgM) compared to healthy individuals
197 (including DD1) using hierarchical clustering. While majority of COVID-19-positive individuals
198 induced high SARS-CoV-2-specific IgM responses, especially to spike antigens, moderate levels of
199 cross-reactive SARS-CoV-2-specific IgM were also detected at high frequencies within the healthy
200 individuals (**Figure 3a**). Similarly, moderate SARS-CoV-2-specific IgA (**Figure 3b**) and IgG (**Figure**
201 **3c**) were observed in healthy individuals, though less frequently than IgM, with cross-reactive IgG
202 responses observed at the lowest frequencies of all isotypes (**Figure 3c**). Overall, moderate levels of
203 SARS-CoV-2 cross-reactive Abs in healthy donors resulted in poor clustering of COVID-19 patients
204 from healthy individuals when a single isotype were assessed, even though multiple SARS-CoV-2
205 antigens were included. This suggests that reported low levels of false positives in current serological
206 diagnostics tests could be due to pre-existing levels of cross-reactive Abs that lead to similar
207 serological signatures as observed in SARS-CoV-2-infected individuals when only quantity of
208 antigen-specific Abs are assessed.
209
210 To identify the minimum Ab signature that best distinguish the COVID-19 patients from healthy
211 individuals, feature selection was used and identified four SARS-CoV-2 Ab variables that
212 differentiated the two groups (**Figure 3d-f**), targeting three different SARS-CoV-2 antigens, S trimer,
213 (fold on stabilized spike ectodomain, 2P mutation¹⁷), NP, and Sclamp (molecular clamp stabilized
214 spike ectodomain¹⁸). Intriguingly, antigen-specific engagement of Fc γ RIIIaV158 and C1q, but not
215 IgG, were selected. This suggests that SARS-CoV-2 infection likely induces antigen-specific Ab with
216 distinct Fc qualities, e.g. Fc glycosylation changes, enhancing binding of Fc γ RIIIaV158 and C1q^{19,20},
217 unlike pre-existing cross-reactive SARS-CoV-2 Abs observed in our healthy donor cohort. In contrast
218 to previous unsupervised hierarchical clustering for IgA, IgM, and IgG (**Figure 3a-c**) to multiple
219 SARS-CoV-2 antigens, these four SARS-CoV-2 Ab features had distinct patterns in COVID-19
220 patients, which lead to the clustering of COVID-19 patients together with a single exception, this

221 notably being the healthy exposed SARS-CoV-2 PCR-negative individual (**Figure 3d**). Strikingly, a
222 supervised PLSDA model of these four features, all associated with COVID-19 patients, could
223 significantly distinguish all COVID-19 patients from healthy individuals on LV1 alone (**Figure 3e**
224 and **f**, $p<0.0001$, $t=34.80$; 98.51% calibration accuracy, 98.51% cross-validation accuracy). To
225 specifically define these four SARS-CoV-2 Ab features, we conducted a correlation network of Ab
226 responses in the COVID-19-positive individuals (**Figure 3g**). High levels of correlation were
227 observed between all SARS-CoV-2 spike antigens: S1, S2, RBD, S Trimer, and Sclamp; while NP
228 antigen-specific Ab features created a separate network. Antigen-specific IgG1 and IgG3, which are
229 the most highly functional IgG subclasses^{21,22}, were the key mediators of FcγR and C1q antigen-
230 specific Ab engagement. Collectively, these results suggest that future COVID-19 serological
231 diagnostic tests could be improved by assessing the Fc quality of antigen-specific Abs in addition to
232 Ab quantity.

233

234 **Convalescent COVID-19 Ab signatures**

235 The majority of COVID-19 moderate/severe samples were collected upon hospital presentation,
236 whereas mild samples were collected upon convalescence (**Extended Data Table 3**). Moreover, there
237 was no significant difference between these groups after adjusting for multiple comparisons, which is
238 not surprising given the small sample size (**Extended Data Table 4**). To explore CoV Ab responses
239 over time, we performed feature selection followed by multivariate regression analysis (PLSR)
240 according to days from first reported disease symptom onset. Not surprisingly, we observed similar
241 Ab signatures to those differentiating healthy from COVID-19 positive individuals, including SARS-
242 CoV-2 antigen-specific Ab engagement with FcγR, C1q, and IgG3 being the most predominant
243 variables associated with convalescence (**Figure 4a-b**, $R^2=0.84$, $Q^2=0.72$), with several of these Ab
244 features individually associated with days from symptom onset (**Extended Data Figure 5**). These
245 data are the first indication that SARS-CoV-2 antigen-specific Ab Fc effector functions may have
246 contributed to convalescent of mild/moderate disease.

247

248 **High SARS-CoV-2 RBD-specific IgM in children**

249 Finally, development of neutralizing Ab responses targeting the RBD are associated with control of
250 SARS-CoV-2, occurs in the majority of convalescent COVID-19 serum samples²³. Therefore,
251 baseline RBD isotype-specific levels between healthy children, adults, elderly and COVID-19 patient
252 plasma samples were assessed via multiplex-assay and validated with published ELISA methods²⁴
253 (**Figure 4c-i-ii, d-i-ii, e-i-ii**). Ab detection in both assays was highly correlated (**Figure 4c-iii, d-iii, e-**
254 **iii**), confirming earlier observations that children induced elevated IgM, while elderly had higher
255 RBD-specific IgA1 responses as measured by multiplex and trended with ELISA IgA results, while
256 no differences in IgG were observed. Since Ab neutralization quality and potency is often correlated
257 with Ab avidity, we therefore conducted urea disassociation assays on a subset of children, elderly

258 and COVID-19 plasma samples (**Figure 4c-iv, 4d-iv**). No differences in IgA avidity were found
259 between children, elderly and COVID-19 patients. Avidity of RBD-specific IgM from elderly was
260 significantly weaker than COVID-19 patients ($p=0.0177$), while children's responses, spanning a
261 large range of avidities, were not significantly different ($p=0.0696$). These data, in combination with
262 the overall higher IgM frequency in children, suggest that children may trend to have more potent
263 RBD-specific IgM which may mature more rapidly upon SARS-CoV-2 exposure, as compared to the
264 elderly.

265

266 Discussion

267 We observed distinct cross-reactive coronavirus serological signatures in healthy children compared
268 to elderly. Children had elevated CoV-specific IgM signatures, whereas elderly had more mature,
269 class-switched CoV-specific IgA and IgG, despite previous epidemiological studies observing higher
270 levels of hCoV infection amongst children compared to the elderly²⁵, indicating that multiple rounds
271 of infections over decades might be needed to develop fully experienced CoV humoral immune
272 responses. Intriguingly, school-aged children often have better clinical outcomes during pandemic
273 influenza outbreaks⁵ and can induce more potent broadly-neutralising Ab upon HIV infection^{26,27}. It is
274 plausible that upon infection with SARS-CoV-2, the elderly may preferentially induce skewed Ab
275 responses targeting prior cross-reactive hCoV antigens, unlike children who have less experienced
276 immunity and are therefore more likely to mount a more targeted immune response to novel antigens
277 from SARS-CoV-2. This immunological phenomenon, known as the Hoskins effect (original antigen
278 sin), observed for several other viral pathogens including influenza and dengue^{28,29} and hypothesized
279 to contribute to enhanced cytokine storm upon dengue reinfection³⁰. These hypotheses will need to be
280 confirmed by future studies examining cross-reactive CoV serological signatures from longitudinal
281 sampling of acute SARS-CoV-2-infected children and elderly.

282

283 Our results indicate HLA-II alleles contribute to differences in Ab signatures prior to antigen
284 exposure, which could potentially impact antigen-specific Ab profiles upon infection, this field has
285 thus far not been studied and could be associated with antigenic sin. Establishment of an effective
286 humoral immune response after infection and vaccination depends on generation of affinity-matured
287 long-lived plasma cells and memory B cells and is correlated with effective activation of T follicular
288 helper (T_{FH}) cells³¹, which depend on the effective presentation of viral epitopes via HLA-II alleles.
289 Several studies demonstrate that variations in HLA-II alleles are associated with susceptibility or
290 resistance to several infectious diseases including MERS-CoV^{32,33} and with vaccine-induced Ab
291 responses³⁴. Due to the low frequency of shared HLA-II alleles, this analysis could not be further
292 explored to determine the contribution of age or sex. However, the clear distinction in Ab signatures
293 emphasizes the need to better understand the contributions of HLA-II alleles to the maturation of

294 humoral immunity and would require a sufficiently large cohort of HLA-typed healthy controls and
295 COVID-19 patients.

296

297 We also assessed the CoV serological profiles of a small cohort of COVID-19 patients, observing
298 distinct SARS-CoV-2 Fc Ab signatures associated with enhanced engagement of Fc γ RIIIaV158 and
299 C1q, distinguishing healthy controls from COVID-19 patients. Ab Fc binding to Fc γ R can be
300 modulated by multiple structural, genetic, and post-translational modifications, including Fc
301 glycosylation^{19,35}. Within convalescent plasma samples, we observed upregulation of SARS-CoV-2
302 antigen-specific IgG, particularly IgG3, which highly correlated with Fc γ R and C1q engagement,
303 suggesting that Fc functional responses may contribute to recovery. Fc effector functions, while
304 beneficial against many pathogens^{15,16,22,36}, can also enhance infection and pathogenesis in other
305 infectious diseases, including dengue, where disease severity is associated with afucosylated IgG1
306 that enhances Fc γ RIIIa affinity³⁷. This is also observed with other respiratory diseases including
307 tuberculosis, where greater overall inflammation, including inflammatory Fc glycosylation is
308 associated with poorer disease outcomes^{36,38}. It is important for future larger SARS-CoV-2 serological
309 studies to assess not only quantitative changes in Ab titers, but also qualitative differences between
310 patients with mild and severe disease, whereas in our study the majority of patients had mild-to-
311 moderate COVID-19.

312

313 Overall, our in-depth serological profiling of healthy children, elderly, and COVID-19 patients brings
314 us closer to understanding why the elderly are more susceptible to COVID-19 and provides insights
315 into Ab Fc signatures associated with convalescence of mild/moderate symptomatic individuals. This
316 knowledge is important for the development of improved serological diagnostics, evaluation of
317 convalescent plasma therapeutic trials and will inform immunogenicity assessment of Ab-based
318 SARS-CoV-2 vaccine strategies which could potentially extend beyond neutralizing Abs.

319

320 **References**

- 321 1 Li, Q. *et al.* Early Transmission Dynamics in Wuhan, China, of Novel Coronavirus-Infected
322 Pneumonia. *N Engl J Med* **382**, 1199-1207, doi:10.1056/NEJMoa2001316 (2020).
- 323 2 University, C. f. S. S. a. E. a. J. H. COVID-19 Dashboard.
- 324 3 Wu, Z. & McGoogan, J. M. Characteristics of and Important Lessons From the Coronavirus
325 Disease 2019 (COVID-19) Outbreak in China: Summary of a Report of 72314 Cases From
326 the Chinese Center for Disease Control and Prevention. *JAMA*, doi:10.1001/jama.2020.2648
327 (2020).
- 328 4 Team, C. C.-R. Severe Outcomes Among Patients with Coronavirus Disease 2019 (COVID-
329 19) - United States, February 12-March 16, 2020. *MMWR Morb Mortal Wkly Rep* **69**, 343-
330 346, doi:10.15585/mmwr.mm6912e2 (2020).
- 331 5 Short, K. R., Kedzierska, K. & van de Sandt, C. E. Back to the Future: Lessons Learned From
332 the 1918 Influenza Pandemic. *Front Cell Infect Microbiol* **8**, 343,
333 doi:10.3389/fcimb.2018.00343 (2018).
- 334 6 Arnold, K. B. & Chung, A. W. Prospects from systems serology research. *Immunology*,
335 doi:10.1111/imm.12861 (2017).

- 336 7 Yasui, F. *et al.* Phagocytic cells contribute to the antibody-mediated elimination of
337 pulmonary-infected SARS coronavirus. *Virology* **454-455**, 157-168,
338 doi:10.1016/j.virol.2014.02.005 (2014).
- 339 8 Yuan, F. F. *et al.* Influence of Fc γ RIIA and MBL polymorphisms on severe acute
340 respiratory syndrome. *Tissue Antigens* **66**, 291-296, doi:10.1111/j.1399-0039.2005.00476.x
341 (2005).
- 342 9 Jaume, M. *et al.* Anti-severe acute respiratory syndrome coronavirus spike antibodies trigger
343 infection of human immune cells via a pH- and cysteine protease-independent Fc γ RI
344 pathway. *J Virol* **85**, 10582-10597, doi:10.1128/JVI.00671-11 (2011).
- 345 10 Liu, L. *et al.* Anti-spike IgG causes severe acute lung injury by skewing macrophage
346 responses during acute SARS-CoV infection. *JCI Insight* **4**, doi:10.1172/jci.insight.123158
347 (2019).
- 348 11 Vabret, N. *et al.* Immunology of COVID-19: current state of the science. *Immunity* **in press**
349 (2020).
- 350 12 Tetro, J. A. Is COVID-19 receiving ADE from other coronaviruses? *Microbes Infect* **22**, 72-
351 73, doi:10.1016/j.micinf.2020.02.006 (2020).
- 352 13 Wines, B. D., Billings, H., McLean, M. R., Kent, S. J. & Hogarth, P. M. Antibody Functional
353 Assays as Measures of Fc Receptor-Mediated Immunity to HIV - New Technologies and their
354 Impact on the HIV Vaccine Field. *Curr HIV Res* **15**, 202-215,
355 doi:10.2174/1570162X15666170320112247 (2017).
- 356 14 McLean, M. R. *et al.* Dimeric Fc γ Receptor Enzyme-Linked Immunosorbent Assay To
357 Study HIV-Specific Antibodies: A New Look into Breadth of Fc γ Receptor Antibodies
358 Induced by the RV144 Vaccine Trial. *J Immunol* **199**, 816-826,
359 doi:10.4049/jimmunol.1602161 (2017).
- 360 15 Chung, A. W. *et al.* Dissecting Polyclonal Vaccine-Induced Humoral Immunity against HIV
361 Using Systems Serology. *Cell* **163**, 988-998, doi:10.1016/j.cell.2015.10.027 (2015).
- 362 16 Vanderven, H. A. *et al.* Antibody-dependent cellular cytotoxicity responses to seasonal
363 influenza vaccination in older adults. *The Journal of infectious diseases* **217**, 12-23 (2017).
- 364 17 Wrapp, D. *et al.* Cryo-EM structure of the 2019-nCoV spike in the prefusion conformation.
365 *Science* **367**, 1260-1263, doi:10.1126/science.abb2507 (2020).
- 366 18 Chappell KJ, D, W. & PR, Y. Chimeric molecules and uses thereof *US Patent App*
367 **16/498,865** (2020).
- 368 19 Chenoweth, A. M., Wines, B. D., Anania, J. C. & Mark Hogarth, P. Harnessing the immune
369 system via Fc γ function in immune therapy: a pathway to next-gen mAbs. *Immunol
370 Cell Biol* **98**, 287-304, doi:10.1111/imcb.12326 (2020).
- 371 20 Goldberg, B. S. & Ackerman, M. E. Antibody-mediated complement activation in pathology
372 and protection. *Immunol Cell Biol* **98**, 305-317, doi:10.1111/imcb.12324 (2020).
- 373 21 Damelang, T., Rogerson, S. J., Kent, S. J. & Chung, A. W. Role of IgG3 in Infectious
374 Diseases. *Trends Immunol* **40**, 197-211, doi:10.1016/j.it.2019.01.005 (2019).
- 375 22 Chung, A. W. *et al.* Polyfunctional Fc-effector profiles mediated by IgG subclass selection
376 distinguish RV144 and VAX003 vaccines. *Sci Transl Med* **6**, 228ra238,
377 doi:10.1126/scitranslmed.3007736 (2014).
- 378 23 Jiang, S., Hillyer, C. & Du, L. Neutralizing Antibodies against SARS-CoV-2 and Other
379 Human Coronaviruses. *Trends Immunol*, doi:10.1016/j.it.2020.03.007 (2020).
- 380 24 Amanat, F. S.; Strohmeier, S.; Nguyen, T.H.O.; Chromikova, V.; McMahon, M.; Jiang,
381 K.; Arunkumar, G.A.; Jurczyszak, D.; Polanco, J.; Bermudez-Gonzalez, M.; Kleiner, G.;
382 Aydillo, T.; Miorin, L.; Fierer, D.; Lugo, L.A.; Kojic, E.M.; Stoever, J.; Liu, S.T.H.;
383 Cunningham-Rundles, C.; Felgner, P.L.; Moran, T.; García-Sastre, A.; Caplivski, D.;
384 Cheng, A.C.; Kedzierska, K.; Vapalahti, O.; Hepojoki, J.M.; Simon, V.; Krammer, F. A
385 serological assay to detect SARS-CoV-2 seroconversion in humans. *Nature Medicine In
386 Press* (2020).
- 387 25 Gaunt, E. R., Hardie, A., Claas, E. C., Simmonds, P. & Templeton, K. E. Epidemiology and
388 clinical presentations of the four human coronaviruses 229E, HKU1, NL63, and OC43
389 detected over 3 years using a novel multiplex real-time PCR method. *J Clin Microbiol* **48**,
390 2940-2947, doi:10.1128/JCM.00636-10 (2010).

- 391 26 Goo, L., Chohan, V., Nduati, R. & Overbaugh, J. Early development of broadly neutralizing
392 antibodies in HIV-1-infected infants. *Nat Med* **20**, 655-658, doi:10.1038/nm.3565 (2014).
- 393 27 Muenchhoff, M. *et al.* Nonprogressing HIV-infected children share fundamental
394 immunological features of nonpathogenic SIV infection. *Sci Transl Med* **8**, 358ra125,
395 doi:10.1126/scitranslmed.aag1048 (2016).
- 396 28 Kim, J. H., Skountzou, I., Compans, R. & Jacob, J. Original antigenic sin responses to
397 influenza viruses. *J Immunol* **183**, 3294-3301, doi:10.4049/jimmunol.0900398 (2009).
- 398 29 Halstead, S. B., Rojanasuphot, S. & Sangkawibha, N. Original antigenic sin in dengue. *Am J*
399 *Trop Med Hyg* **32**, 154-156, doi:10.4269/ajtmh.1983.32.154 (1983).
- 400 30 Rothman, A. L. Immunity to dengue virus: a tale of original antigenic sin and tropical
401 cytokine storms. *Nat Rev Immunol* **11**, 532-543, doi:10.1038/nri3014 (2011).
- 402 31 Koutsakos, M. *et al.* Circulating TFH cells, serological memory, and tissue
403 compartmentalization shape human influenza-specific B cell immunity. *Sci Transl Med* **10**,
404 doi:10.1126/scitranslmed.aan8405 (2018).
- 405 32 Thursz, M. R. *et al.* Association between an MHC class II allele and clearance of hepatitis B
406 virus in the Gambia. *N Engl J Med* **332**, 1065-1069, doi:10.1056/NEJM199504203321604
407 (1995).
- 408 33 Hajeer, A. H., Balkhy, H., Johani, S., Yousef, M. Z. & Arabi, Y. Association of human
409 leukocyte antigen class II alleles with severe Middle East respiratory syndrome-coronavirus
410 infection. *Ann Thorac Med* **11**, 211-213, doi:10.4103/1817-1737.185756 (2016).
- 411 34 Ovsyannikova, I. G., Pankratz, V. S., Vierkant, R. A., Jacobson, R. M. & Poland, G. A.
412 Human leukocyte antigen haplotypes in the genetic control of immune response to measles-
413 mumps-rubella vaccine. *J Infect Dis* **193**, 655-663, doi:10.1086/500144 (2006).
- 414 35 Chung, A. W. *et al.* Identification of antibody glycosylation structures that predict
415 monoclonal antibody Fc-effector function. *AIDS* **28**, 2523-2530,
416 doi:10.1097/QAD.0000000000000444 (2014).
- 417 36 Lu, L. L. *et al.* A Functional Role for Antibodies in Tuberculosis. *Cell* **167**, 433-443 e414,
418 doi:10.1016/j.cell.2016.08.072 (2016).
- 419 37 Wang, T. T. *et al.* IgG antibodies to dengue enhanced for FcgammaRIIA binding determine
420 disease severity. *Science* **355**, 395-398, doi:10.1126/science.aai8128 (2017).
- 421 38 McLean, M. R., Lu, L. L., Kent, S. J. & Chung, A. W. An Inflammatory Story: Antibodies in
422 Tuberculosis Comorbidities. *Front Immunol* **10**, 2846, doi:10.3389/fimmu.2019.02846
423 (2019).
- 424

425 **Figure Legends**

426 **Figure 1. Vastly different serological signatures between children and elderly**

427 (a) Volcano plot of children (orange) versus elderly (dark blue), open circles are not significantly
428 different between two groups. Data was zscored prior to analysis. (b) PCA of all 196 Ab features for
429 healthy children, adults (light blue square), and elderly. PLSDA scores (c) and loadings plots (d)
430 using the 15-feature Elastic-Net selected signature for children versus elderly (0.88% calibration
431 error, 1.44% cross-validation error). Variance explained on each LV is in parentheses. Statistically
432 significant separation of groups was determined using a two-tailed t-test on LV1 scores $p<0.0001$, $t =$
433 21.60 (e) Hierarchical clustering of Elastic-Net selected features for children and elderly. Levels are
434 coloured from low (dark blue) to high (dark red). Correlation network analyses for children (f) and
435 elderly (g) identify features associated with the Elastic-Net selected features (red outline). Coded by
436 Ab feature type (colour), antigen (shape), correlation strength (line thickness, alpha <0.05), and
437 correlation coefficient (line colour).

439 **Figure 2. HLA-II alleles influence Ab signatures**

440 HLA-DQB1, -DRB1 and -DPB1 alleles in our healthy donor cohort (a,d,g), PLSDA scores (b,e,h) and
441 loadings (c,f,i) plots using the Elastic-Net selected signatures for the two most frequent alleles (HLA-
442 DQB1*03:01 and 06:02, 17.41% cross-validation error, 13.56% calibration error; HLA-DRB1*15:01
443 and 07:01, 23.68% cross-validation error, 20.17% calibration error; HLA-DPB1*04:01 and 02:01,
444 25.78% cross-validation error, 17.66% calibration error). Variance explained on each LV is in
445 parentheses. Analysis was performed on a subset of the healthy individuals (n=111) for whom HLA
446 class II type was available. Donors heterozygotes for the two most frequent HLA alleles were
447 excluded from PLSDA and loading analysis.

448

449 **Figure 3. Healthy versus COVID-19 serological signatures**

450 Hierarchical clustering of all SARS-CoV-2 antigens for IgM (a), IgA1 (b) and IgG (c). Levels are
451 coloured from low (dark blue) to high (dark red). Hierarchical clustering (d) and PLSDA model
452 scores (e) and loadings (f) were performed using the four-feature Elastic-Net selected SARS-CoV-2
453 antigen signature (1.49% calibration error, 1.49% cross-validation error). Variance explained by each
454 LV is in parentheses. (g) Correlation network analysis for COVID-19 patients was performed to
455 identify features significantly associated with the Elastic-Net selected features (red outline). Coded by
456 Ab feature type (colour), antigen (shape), correlation strength (line thickness, alpha <0.05) and
457 correlation coefficient (line colour). Data was zscored prior to analysis.

458

459 **Figure 4. COVID-19 Ab responses over time and RBD Abs in healthy versus COVID-19**

460 PLSR model scores plot (a) loadings plot (b) for all COVID-19 patient data on Elastic-Net 15-feature
461 signature. The model goodness of fit (R^2) was 0.8361 and goodness of predication (Q^2) was 0.7194.
462 Percent variance explained by each latent variable in parenthesis. Multiplex MFI data for IgM (c-i),
463 IgA (d-i) and IgG (e-i), ELISA endpoint titers for IgM (c-ii), IgA (d-ii) and IgG (e-ii), and their
464 respective correlations (c-e iii). Avidity index following urea dissociation for IgM (c-iv) and, IgA (d-
465 iv). Children (orange), adults (light blue), elderly (dark blue) and COVID-19 patients (red). Bar
466 indicates the median response of each group. Statistical significance was determined using-Kruskal
467 Wallis with Dunn's multiple comparisons, exact p-values are provided.

468

469

470 **Materials and Methods**

471 **Study participants and sample collection**

472 Our study assessed antibodies to SARS-CoV-2 in a total of 244 healthy individuals and 19 SARS-
473 CoV-2-infected patients (**Extended Data Figure 2a, Table 1 and 3**). Children undergoing elective
474 tonsillectomy (age 1.5-19) were recruited at the Launceston General Hospital (Tasmania) and, apart
475 from fulfilling the criteria for tonsillectomy, they were considered otherwise healthy, showing no
476 signs of immune compromise. Healthy adult donors (age 22-63) were recruited via the University of

477 Melbourne. Healthy elderly donors (age 65-92) were recruited at the Deepdene Medical Clinic
478 (Victoria). All healthy donors were recruited prior to SARS-CoV-2 pandemic. SARS-CoV-2-infected
479 patients (age 21-75) were recruited at the Alfred Hospital (AH). Convalescent individuals who
480 recovered from COVID-19 were recruited by James Cook University (DD) or University of
481 Melbourne (CP). Eligibility criteria for COVID-19- acute and convalescent recruitment were age ≥ 18
482 years old and having at least one swab PCR-positive for SARS-CoV-2. Each patient was categorized
483 into one of the following 6 severity categories: very mild (stay at home minimal symptoms), mild
484 (stay at home with symptoms), moderate (hospitalized, not requiring oxygen), severe/moderate
485 (hospitalized with low flow oxygen), severe (hospitalized with high flow oxygen) or critical (intensive
486 care unit (ICU)). Heparinised blood was centrifuged for 10 min at 300 g to collect plasma, which was
487 frozen at -20°C until required. HLA class I and class II molecular genotyping was performed from
488 genomic DNA by the Australian Red Cross Lifeblood (Melbourne).

489

490 Human experimental work was conducted according to the Declaration of Helsinki principles and
491 according to the Australian National Health and Medical Research Council Code of Practice. All
492 donors or their legal guardians provided written informed consent. The study was approved by the
493 Human Research Ethics Committee (HREC) of the University of Melbourne (Ethics ID #1443389.4,
494 #2056761, #1647326, #2056689, #1955465) for healthy adult and elderly donors, Tasmanian Health
495 and Medical HREC (H0017479) for healthy child donors, Alfred Hospital (#280/14) for AH donors,
496 James Cook University (#H7886) for DD donors and University of Melbourne (#2056689) for CP
497 donors.

498

499 **Deglycosylation of *E. coli*-expressed NP**

500 To minimise background from the *E. coli* expression system, recombinant hCoV 229E and NL63 NP
501 (Prospec-Tany) were first treated with O-glycosidase and PNGase F. Briefly, 40 μ g of NP were treated
502 with a cocktail of 8 μ l 10X GlycoBuffer 2, 8 μ l 10% NP40, 12 μ l O-Glycosidase, 12 μ l of Remove-iT
503 PNGase F (New England BioLabs) and water for a final volume of 80 μ l and incubated at 37°C for
504 two hours on a shaker. The respective mixtures were added to Eppendorf tubes containing 100 μ l of
505 PBS-washed Chitin magnetic beads (New England BioLabs) to allow the binding and removal of
506 Remove-iT PNGase F. Tubes were agitated for 10 minutes then placed onto a magnetic separation
507 rack for 5 minutes. The supernatant was retrieved and passed through a 100kDa Amicon Ultra
508 centrifugal filter (Merck) to remove remaining O-glycosidase. Finally, NPs were washed with PBS
509 using a 3kDa Amicon Ultra centrifugal filter (Merck) to prepare them for coupling.

510

511 **Coupling of carboxylated beads**

512 A custom CoV multiplex assay was designed with SARS-CoV-2, SARS-CoV-1, MERS-CoV and
513 hCoV (229E, HKU1, NL63) S and NP antigens, as well as SARS-CoV-2 RBD (gift from Florian

514 Krammer)²⁴, SARS-CoV-2 Trimeric S (gift from Adam Wheatley) and SClamps of both SARS-CoV-
515 2 and MERS-CoV (gift from University of Queensland) (**Extended Data Figure 1b**). Tetanus toxoid
516 (Sigma) and influenza hemagglutinin (H1Cal2009; Sino Biological), were also added to the assay as
517 positive controls, while BSA blocked beads were included as negative controls. Magnetic
518 carboxylated beads (Bio Rad) were covalently coupled to the antigens using a two-step carbodiimide
519 reaction, in a ratio of 10 million beads to 100µg of antigen, with the exception of the deglycosylated
520 NPs mentioned above in which 40µg were used instead. Briefly, beads were washed and activated in
521 100 mM monobasic sodium phosphate, pH 6.2, followed by the addition of Sulfo-N-
522 hydroxysulfosuccinimide and 1-Ethyl-3-(3-dimethylaminopropyl) carbodiimide (Thermo Fisher
523 Scientific). After incubation at room temperature (RT) for 30 minutes, the activated microspheres
524 were washed three times and resuspended in 50mM MES pH 5.0 (Thermo Fisher Scientific). The
525 respective antigens were added to the activated beads and the mixture was incubated at RT for three
526 hours on a rotator in the dark. Subsequently, the beads were washed with PBS and blocked with
527 blocking buffer (PBS, 0.1% BSA, 0.02% TWEEN-20, 0.05% Azide, pH 7) for 30 minutes. Finally,
528 beads were washed in PBS 0.05% Sodium Azide and resuspended to one million beads per 100µl.
529

530 **Luminex bead-based multiplex assay**

531 The isotypes and subclasses of pathogen-specific antibodies present in the collected plasma were
532 assessed using a multiplex assay as described³⁹. Using a black, clear bottom 384-well plate (Greiner
533 Bio-One), 20µl of working bead mixture containing 1000 beads per bead region and 20µl of diluted
534 plasma were added per well. From validation experiments in which cross-reactive Abs present in
535 healthy individuals were titrated, an optimal concentration of 1:100 working dilution of plasma was
536 selected for downstream assays (**Extended data Figure 1c and d**). The plate was covered and
537 incubated overnight at 4°C on a shaker and was then washed with PBS containing 0.05% Tween20
538 (PBST). Pathogen-specific antibodies were detected using phycoerythrin (PE)-conjugated mouse anti-
539 human pan-IgG, IgG1-4, IgA1-2 (Southern Biotech), at 1.3µg/ml, 25µl per well. After incubation at
540 RT for two hours on a shaker, the plate was washed, before the beads were resuspended in 50 µl of
541 sheath fluid. The plate was then incubated at RT for 10 minutes on a shaker before being read by the
542 FlexMap 3D. The binding of the PE-detectors was measured to calculate the median fluorescence
543 intensity (MFI). Double background subtraction was conducted, removing first background of blank
544 (buffer only) wells followed by removal of BSA-blocked control bead background signal for each
545 well.
546

547 For the detection of IgM, biotinylated mouse anti-human IgM (mAb MT22; MabTech) was added at
548 1.3µg/ml, 25µl per well. After incubation at RT for two hours on a shaker, the plate was washed, and
549 streptavidin, R-Phycoerythrin conjugate (SAPE; Invitrogen) was added at 1µg/ml, 25µl per well. The
550 plate was then incubated at RT for two hours on a shaker before being washed and read as mentioned

551 above. For the detection of Fc γ R, soluble recombinant Fc γ R dimers (higher affinity polymorphisms
552 Fc γ RIIa-H131, lower affinity polymorphisms Fc γ RIIa-R131, Fc γ RIIb, higher affinity polymorphisms
553 Fc γ RIIIa-V158, lower affinity polymorphisms Fc γ RIIIa-F158) were provided by Bruce Wines and
554 Mark Hogarth. For the detection of C1q, C1q protein (MP Biomedicals) was first biotinylated
555 (Thermo Fisher Scientific), washed and resuspended in PBS and tetramerized with SAPE. Dimers or
556 tetrameric C1q-PE were added at 1 μ g/ml, 25 μ l per well, incubated at RT for two hours on a shaker,
557 then washed. For Dimers, SAPE was added at 1 μ g/ml, 25 μ l per well, incubated at RT for two hours
558 on a shaker before being washed and read as mentioned above. Assays were repeated in duplicate. A
559 titration of AH0073 was included in the layout of all multiplex array plates as this patient was known
560 to have IgG, IgM and IgA responses (**Extended Data Figure 6**). These titrations were used to
561 normalize replicate multiplex array plates.

562

563 **Enzyme-linked immunosorbent assay (ELISA)**

564

565 Detection of RBD-specific antibodies was performed as described in Stadlbauer et al^{24,40} with the
566 following modifications; Nunc MaxiSorp flat bottom 96-well plates (Thermo Fisher Scientific) were
567 used for antigen coating, blocking performed with PBS containing 10% BSA and serial dilutions
568 performed with PBST containing 5% BSA. For detection of IgG and IgA, peroxidase-conjugated goat
569 anti-human IgG (Fc γ fragment specific; Jackson ImmunoResearch) or alkaline phosphate-conjugated
570 rat anti-human IgA (mAb MT20; MabTech), was used and developed with TMB (Sigma) substrate for
571 IgG or pNPP (Sigma) for IgA. For IgM, biotinylated mAb MT22 and peroxidase-conjugated
572 streptavidin (Pierce; Thermo Fisher Scientific) was used. Peroxidase reactions were stopped using 1M
573 H₃PO₄ and plates read at 450nm or 405nm on a Multiskan plate reader (Labsystems). All
574 measurements were normalised using a positive control plasma from a COVID-19 patient (AH0073)
575 run on each plate (**Extended data Figure 6**). Endpoint titres were determined by interpolation from a
576 sigmoidal curve fit (all R-squared values >0.95; GraphPad Prism 8) as the reciprocal dilution of
577 plasma that produced \geq 15% absorbance of the positive control. A total of 28 donors from each cohort
578 was randomly selected for IgA analysis, 14 for IgG and 10-14 for IgM. All assays also included 5
579 same COVID-19 patient samples.

580

581 **Antibody avidity assay**

582

583 Avidity of antibodies in plasma samples was measured using urea as the chaotropic agent and only
584 performed on samples with detectable RBD-specific antibodies (IgA and IgM). Following incubation
585 of plasma at a 1:10 dilution (IgA) or 1:100 dilution (IgM) on RBD-coated plates, 6M of urea was
586 added and incubated for 15 minutes. Bound antibodies were then detected using respective secondary
587 detection reagents described above. The avidity index is expressed as the percentage of remaining
588 antibody bound to antigen following urea treatment compared to the absence of urea.

588

589 Statistical Analysis

590 Children versus the elderly Volcano plot was conducted using Prism 8. Statistical significance
591 determined using the Holm-Sidak method, with alpha = 0.05 adjusted for 196 tests (Ab features). Each
592 feature was analyzed individually, without assuming a consistent SD. The overall multiplex dataset was
593 analysed for normal distribution using the Shapiro-Wilk test by Prism 8. The data were further
594 analysed by SPSS statistics 26 (IBM Corp.) using the Kruskal-Wallis one-way analysis with a
595 Bonferroni correction to determine the p-values, differences between groups were considered
596 significant at an adjusted p-value of 0.000035 (**Extended data Table 2**). ELISA data was analyzed
597 using Kruskal-Wallis one-way analysis with Dunn's multiple comparison using Prism 8. Differences
598 between very mild/mild and moderate/severe/critical patients were analysed using the Mann-Whitney
599 test and differences were considered significant at a *p*-value of 0.05 (**Extended data Table 4**).
600

601 Data Normalization

602 For all multivariate analysis Tetanus, H1Cal2009 antigens (positive controls) were removed, with the
603 exception of HLA analysis. Any healthy samples with a missing age, or missing Ab features were
604 removed (n=9). When analysing COVID-19 samples with healthy samples, only the features where
605 data was available for all COVID-19 samples were included. COVID-19 samples lacked entire
606 datasets for IgG4, IgA2, FcgRIIaR131, FcgRIIIaF158, and FcgRIIb, thus these detectors were
607 excluded. When COVID-19 samples were analysed based on the time from disease onset, all visit
608 days were used for each patient. In all other analyses when a patient has two visit days only the
609 second visit was used. Right shifting was performed on each feature (detector-antigen pair)
610 individually if it contained any negative values, by adding the minimum value for that feature back to
611 all samples within that feature. Following this all data was log transformed using the following
612 equation, where x is the right shifted data and y is the right shifted log transformed data: $y = \log_{10}(x+1)$. This process transformed the majority of the features to having a normal distribution. In
613 all subsequent multivariate analysis, the data were furthered normalized by mean centring and
614 variance scaling each feature using the zscore function in Matlab. For the HLA analysis, the same
615 data normalization methods were used, except that positive controls were included and all samples
616 with any HLA typing were included. Samples with one copy of each most frequent allele were
617 removed to avoid double classification.
618

619

620 Feature Selection Using Elastic Net/PLSR and Elastic Net/PLSDA

621 To determine the minimal set of features (signatures) needed to predict numerical outcomes (age, days
622 from symptom onset) and categorical outcomes (age cohort, COVID-19 infection status, HLA Allele)
623 a three-step process was developed based on⁴¹. First, the data were randomly sampled without
624 replacement to generate 2000 subsets. The resampled subsets spanned 80% of the original sample

size, or sampled all classes at the size of the smallest class for categorical outcomes, which corrected for any potential effects of class size imbalances during regularization. Elastic-Net regularization was then applied to each of the 2000 resampled subsets to reduce and select features most associated with the outcome variables. The Elastic-Net hyperparameter, alpha, was set to have equal weights between the L1 norm and L2 norm associated with the penalty function for least absolute shrinkage and selection (LASSO) and ridge regression, respectively⁴². By using both penalties, Elastic-Net provides sparsity and promotes group selection. The frequency at which each feature was selected across the 2000 iterations was used to determine the signatures by using a sequential step-forward algorithm that iteratively added a single feature into the PLSR (numerical outcome) or PLSDA (categorical outcome) model starting with the feature that had the highest frequency of selection, to the lowest frequency of selection. Model prediction performance was assessed at each step and evaluated by 10-fold cross-validation classification error for categorical outcomes and 10-fold goodness of prediction (Q^2) for numerical outcomes. The model with the lowest classification error and highest Q^2 within a 0.01 difference between the minimum classification error or the maximum Q^2 were selected as the minimum signature. If multiple models fell within this range, the one with the least number of features was selected and if there was a large disparity between calibration and cross-validation error (overfitting), the model with the least disparity and best performance was selected.

642

643 **PCA**

644 Principal Component Analysis (PCA), performed in Eigenvectors PLS toolbox in Matlab, is an
645 unsupervised technique that was used to visualize the variance in the samples based on all of the
646 measured features. Every feature is assigned a loading, the linear combinations of these loadings
647 creates a principal component (PC). Loadings and principal components are calculated to describe the
648 maximum amount of variance in the data. Each sample is then scored and plotted using their
649 individual response measurements expressed through the PCs. The percent of variance described by
650 each PC is a measure of the amount of variance in antibody response explained by that respective PC.
651 Separation of groups on the scores plot indicates unsupervised separation of groups based on all
652 features.

653

654 **PLSDA**

655 Partial Least Squares Discriminant Analysis (PLSDA), performed in Eigenvectors PLS toolbox in
656 Matlab, was used in conjunction with Elastic-Net, described above, to identify and visualize
657 signatures that distinguish categorical outcomes (age cohort, COVID-19 infection status). This
658 supervised method assigns a loading to each feature within a given signature and identifies the linear
659 combination of loadings (a latent variable) that best separates the categorical groups. A feature with a
660 high loading magnitude indicates greater importance for separating the groups from one another. Each
661 sample is then scored and plotted using their individual response measurements expressed through the

662 latent variables (LVs). The scores and loadings can then be cross referenced to determine which
663 features are loaded in association with which categorical groups (positively loaded features are higher
664 in positively scoring groups etc). All models go through 10-fold cross-validation, where iteratively
665 10% of the data is left out as the test set, and the rest is used to train the model. Model performance is
666 measured through calibration error (average error in the training set) as well as cross-validation error
667 (average error in the test set), with values near zero being best. All models were orthogonalized to
668 enable clear visualization of results. Statistically significant separation of groups on the PLSDA score
669 plots was determined using a two-tailed t-test on LV1 scores in Prism 8.

670

671 **PLSR**

672 Partial Least Squares Regression (PLSR), performed in Eigenvectors PLS toolbox in Matlab, was
673 used in conjunction with Elastic-Net, described above, to identify and visualize signatures that
674 distinguish numerical outcomes (age, days from symptom onset). This supervised method assigns a
675 loading to each feature within a given signature and identifies the linear combination of loadings (a
676 latent variable) that best describes the variance in the numerical outcome. As in PLSDA, a feature
677 with a high loading indicates greater importance for describing the variance in outcome. Each sample
678 is then scored and plotted using their individual response measurements expressed through the latent
679 variables (LVs). The scores and loadings can then be cross referenced to determine which features are
680 loaded in association with which numerical outcomes (positively loaded features are higher in
681 positively scoring samples etc). All models go through 10-fold cross validation, where iteratively 10%
682 of the data is left out as the test set, and the rest is used to train the model. Model performance is
683 measured through R^2 (average goodness of fit in the training set) as well as Q^2 (average goodness of
684 prediction in the test set), with values near 1 being best. All models were orthogonalized to enable
685 clear visualization of results.

686

687 **Hierarchical Clustering**

688 We visualized separation of numerical (age, days from symptom onset) and categorical (age cohort,
689 COVID-19 infection status) outcomes based on their respective signatures using unsupervised average
690 linkage hierarchical clustering of normalized data; Euclidean distance was used as the distance
691 metric.

692

693 **Multiple sequence alignment of CoV Spike and NP**

694 FASTA sequences were obtained from Genpept using the accession numbers as provided by the
695 companies (**Extended data Figure 1b**). Sequences were cut in Jalview 2.10.5 and subsequently
696 aligned using T-Coffee with the default settings. Residues were coloured to display consensus to the
697 S1 and NP of SAR-CoV-2. Distance matrix for multiple alignment similarities were made in Ugene.

698

699 **Software**

700 PCA, PLSDA, and PLSR models were completed using the Eigenvector PLS toolbox in Matlab.
701 Hierarchical Clustering and Correlation Networks were completed using MATLAB 2017b
702 (MathWorks, Natick, MA). PCA, PLSDA, and PLSR scores and loadings plots were plotted in Prism
703 version. Statistical analysis were performed in SPSS. Multiple sequence alignment was done in
704 Jalview 2.10.5 and distance matrix for multiple alignments was done in Ugene 1.16.1
705 (<http://ugene.unipro.ru>; Unipro, Novosibirsk, Russia).

706

707 **Data availability**

708 The source data underlying Figs 1-4, Extended data Figs 1, 2, 4, 5, 6, Extended Data table 2 and 4 are
709 provided as a Source Data file. The coding used for analysis can be found in the Source Coding file.
710 All other data are available from the authors upon request.

711

712

713 **References**

- 714 39 Brown, E. P. *et al.* High-throughput, multiplexed IgG subclassing of antigen-specific
715 antibodies from clinical samples. *Journal of immunological methods* **386**, 117-123,
716 doi:10.1016/j.jim.2012.09.007 (2012).
717 40 Stadlbauer, D. *et al.* SARS-CoV-2 Seroconversion in Humans: A Detailed Protocol for a
718 Serological Assay, Antigen Production, and Test Setup. *Curr Protoc Microbiol* **57**, e100,
719 doi:10.1002/cpmc.100 (2020).
720 41 Gunn, B. M. *et al.* Enhanced binding of antibodies generated during chronic HIV infection to
721 mucus component MUC16. *Mucosal Immunol* **9**, 1549-1558, doi:10.1038/mi.2016.8 (2016).
722 42 Zou, H. & Hastie, T. Regularization and variable selection via the elastic net. *Journal of the
723 Royal Statistical Society: Series B (Statistical Methodology)* **67**, 301-320, doi:10.1111/j.1467-
724 9868.2005.00503.x (2005).
725

726

727 **Acknowledgments**

728 We thank all the participants involved in the study, Ebene Haycroft and Brendan Watts for
729 Flexmap3D technical assistance. This work was supported by Jack Ma Foundation to KK, AWC and
730 AW, the Clifford Craig Foundation to KLF and KK, NHMRC Leadership Investigator Grant to KK
731 (1173871), NHMRC Program Grant to KK (1071916), NHMRC Program Grant to DLD (#1132975),
732 NHMRC program grant to SJK (#1149990), Research Grants Council of the Hong Kong Special
733 Administrative Region, China (#T11-712/19-N) to KK. AWC is supported by a NHMRC Career
734 Development Fellowship (#1140509), KK by NHMRC Senior Research Fellowship (1102792), DLD
735 by a NHMRC Principal Research Fellowship (#1137285). SJK by NHMRC Senior Principal Research
736 Fellowship (#1136322). CES has received funding from the European Union's Horizon 2020 research
737 and innovation program under the Marie Skłodowska-Curie grant agreement No 792532. LH is
738 supported by the Melbourne International Research Scholarship (MIRS) and the Melbourne

739 International Fee Remission Scholarship (MIFRS) from The University of Melbourne. JAJ is
740 supported by an NHMRC Early Career Fellowship (ECF) (APP1123673)

741

742 **Author Contributions**

743 KJS, CES, BYC, THON, JC, KLF, ACC, DLD, DCJ, SJK, KBA, KK and AWC formulated ideas,
744 designed the study and experiments; KJS, CES, BYC, THON, LR, LH, MK, CYW, RE, HGK, HXT,
745 JAJ, AKW and AWC performed experiments; FA, FK, KC, NM, DW, PY, BW, PMH and AKW
746 contributed unique reagents; KJS, CES, MML, CYL, SKS, BYC and AWC analysed the experimental
747 data; KJS, CES, MML, CYL, SKS, BYC, KK and AWC wrote the manuscript. All authors reviewed
748 the manuscript.

749

750 **Conflict of interest statement**

751 Authors declare no conflict of interest.

752 **Additional information**

753 Supplementary information is available for this paper

754 Correspondence and requests for materials should be addressed to Katherine Kedzierska and Amy
755 Chung.

756

757 **Supplementary information**

758 **Figure Legends**

759 **Figure 1. Vastly different serological signatures between children and elderly**

760 (a) Volcano plot of children (orange) versus elderly (dark blue), open circles are not significantly
761 different between two groups. Data was zscored prior to analysis. (b) PCA of all 196 Ab features for
762 healthy children, adults (light blue square), and elderly. PLSDA scores (c) and loadings plots (d)
763 using the 15-feature Elastic-Net selected signature for children versus elderly (0.88% calibration
764 error, 1.44% cross-validation error). Variance explained on each LV is in parentheses. Statistically
765 significant separation of groups was determined using a two-tailed t-test on LV1 scores $p < 0.0001$, $t =$
766 21.60 (e) Hierarchical clustering of Elastic-Net selected features for children and elderly. Levels are
767 coloured from low (dark blue) to high (dark red). Correlation network analyses for children (f) and
768 elderly (g) identify features associated with the Elastic-Net selected features (red outline). Coded by
769 Ab feature type (colour), antigen (shape), correlation strength (line thickness, alpha < 0.05), and
770 correlation coefficient (line colour).

771

772 **Figure 2. HLA-II alleles influence Ab signatures**

773 HLA-DQB1, -DRB1 and -DPB1 alleles in our healthy donor cohort (a,d,g), PLSDA scores (b,e,h) and
774 loadings (c,f,i) plots using the Elastic-Net selected signatures for the two most frequent alleles (HLA-
775 DQB1*03:01 and 06:02, 17.41% cross-validation error, 13.56% calibration error; HLA-DRB1*15:01
776 and 07:01, 23.68% cross-validation error, 20.17% calibration error; HLA-DPB1*04:01 and 02:01,

777 25.78% cross-validation error, 17.66% calibration error). Variance explained on each LV is in
778 parentheses. Analysis was performed on a subset of the healthy individuals (n=111) for whom HLA
779 class II type was available. Donors heterozygotes for the two most frequent HLA alleles were
780 excluded from PLSDA and loading analysis.

781

782 **Figure 3. Healthy versus COVID-19 serological signatures**

783 Hierarchical clustering of all SARS-CoV-2 antigens for IgM (a), IgA1 (b) and IgG (c). Levels are
784 coloured from low (dark blue) to high (dark red). Hierarchical clustering (d) and PLSDA model
785 scores (e) and loadings (f) were performed using the four-feature Elastic-Net selected SARS-CoV-2
786 antigen signature (1.49% calibration error, 1.49% cross-validation error). Variance explained by each
787 LV is in parentheses. (g) Correlation network analysis for COVID-19 patients was performed to
788 identify features significantly associated with the Elastic-Net selected features (red outline). Coded by
789 Ab feature type (colour), antigen (shape), correlation strength (line thickness, alpha <0.05) and
790 correlation coefficient (line colour). Data was zscored prior to analysis.

791

792 **Figure 4. COVID-19 Ab responses over time and RBD Abs in healthy versus COVID-19**

793 PLSR model scores plot (a) loadings plot (b) for all COVID-19 patient data on Elastic-Net 15-feature
794 signature. The model goodness of fit (R^2) was 0.8361 and goodness of predication (Q^2) was 0.7194.
795 Percent variance explained by each latent variable in parenthesis. Multiplex MFI data for IgM (c-i),
796 IgA (d-i) and IgG (e-i), ELISA endpoint titers for IgM (c-ii), IgA (d-ii) and IgG (e-ii), and their
797 respective correlations (c-e iii). Avidity index following urea dissociation for IgM (c-iv) and, IgA (d-
798 iv). Children (orange), adults (light blue), elderly (dark blue) and COVID-19 patients (red). Bar
799 indicates the median response of each group. Statistical significance was determined using-Kruskal
800 Wallis with Dunn's multiple comparisons, exact p-values are provided.

801

802 **Extended Data Figure 1. Multiplex Assay setup and optimization**

803 (a-i-iii) Schematic of bead-based multiplex assay. (b) Overview of antigens included in the assay. (c)
804 Multiplex was validated by measuring a subset of healthy samples both in singleplex and multiplex.
805 Strong correlations suggest that multiplexing did not affect measurement of Ab responses, especially
806 at 1:50 and 1:100 dilutions. (d) Serial dilution of a subset of healthy samples against 14 antigens
807 included in the custom multiplex assay to select dilutions where saturation was not observed. A final
808 dilution of 1: 100 showed not only strong correlation between singleplexed and multiplexed antigens,
809 but was also not saturated for most antigens and was selected for subsequent assays.

810

811 **Extended Data Figure 2. Age versus CoV Ab responses**

812 (a) Overview of the healthy donors per age groups and COVID-19 patients. PLSR model scores plot
813 (b) loadings plot (c) for all healthy patient data on Elastic-Net 11-feature signature. The model

814 goodness of fit (R^2) was 0.6421 and goodness of predication (Q^2) was 0.6144. Percent variance
815 explained by each latent variable in parenthesis. (d) Hierarchical clustering of signature in (b-c). (e)
816 Spearman correlation was performed to associate age with the strength of Ab features against the six
817 SARS-CoV-2 antigens.

818

819 **Extended Data Figure 3. Multiple Sequence alignment of NP and S1**

820 Amino acid sequence alignments of the various NP (a) and S1 (b) used in the assay. Fasta sequences
821 were obtained from Genpept and aligned using T-Coffee with default settings. Amino acids were
822 highlighted to show consensus towards the SARS-CoV-2 proteins, with darker shades of blue being
823 used with increasing consensus. (c) Percentage amino acid sequence alignment for NP and S1
824 between SARS-CoV-2 and SARS-CoV-1, MERS, hCoV NL63, 229E and HKU1.

825

826 **Extended Data Figure 4. SARS2 Ab titrations**

827 Serial dilutions of COVID-19 plasmas against the six SARS-CoV-2 antigens in the assay. Very mild
828 and mild cases were coloured black, while moderate to severe cases were coloured orange. For
829 comparison, two healthy elderly plasma were included (green). DD1, who was SARS CoV-2-exposed
830 but remained SARS CoV-2 PCR-negative, was also included (purple).

831

832 **Extended Data Figure 5. Time from symptom onset and Ab responses**

833 Antibody features against SARS-CoV-2 antigens which associate with the time of onset of COVID-
834 19, as analysed through Spearman correlation, are displayed. Very mild and mild cases are displayed
835 as black squares while moderate to critical cases are displayed as orange diamonds.

836

837 **Extended Data Figure 6: ELISA plasma titrations**

838 Serial dilutions of plasma from healthy children (n=14) (orange), 12 adults (n=12) (light blue), 14
839 elderly (n=14) (dark blue) and 5 COVID-19 patients (red) tested in IgM (a), IgA (b) and IgG (c)
840 ELISA. Bold red line represents COVID-19 patient AH0073 who was used as a positive control in all
841 multiples and ELISA plates. Dashed lines represent cut-offs (15% of positive control for IgA and IgG;
842 30% for IgM) used to interpolate end point titers by non-linear regression analysis.

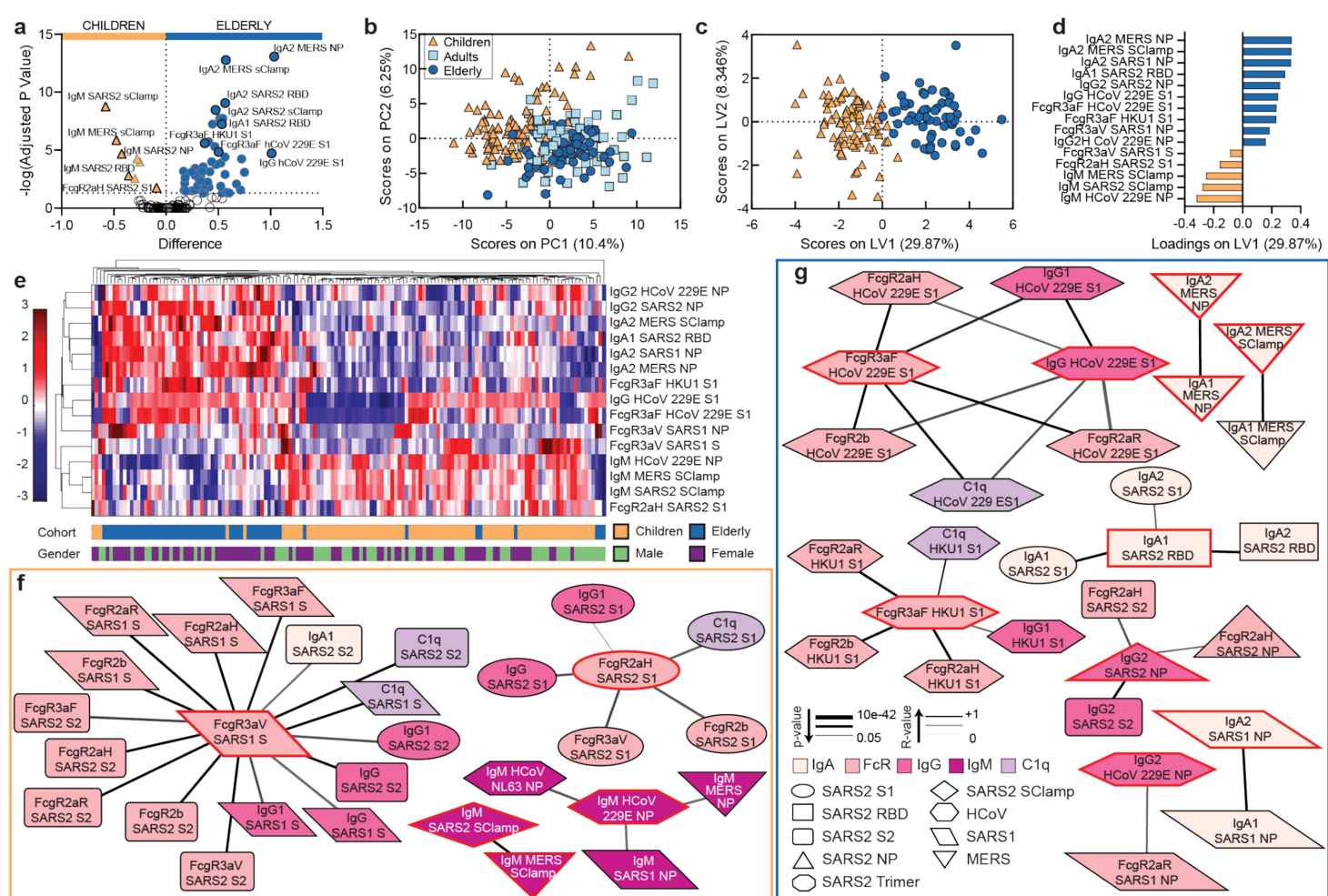


Figure 1 Vastly different serological signatures between children and elderly

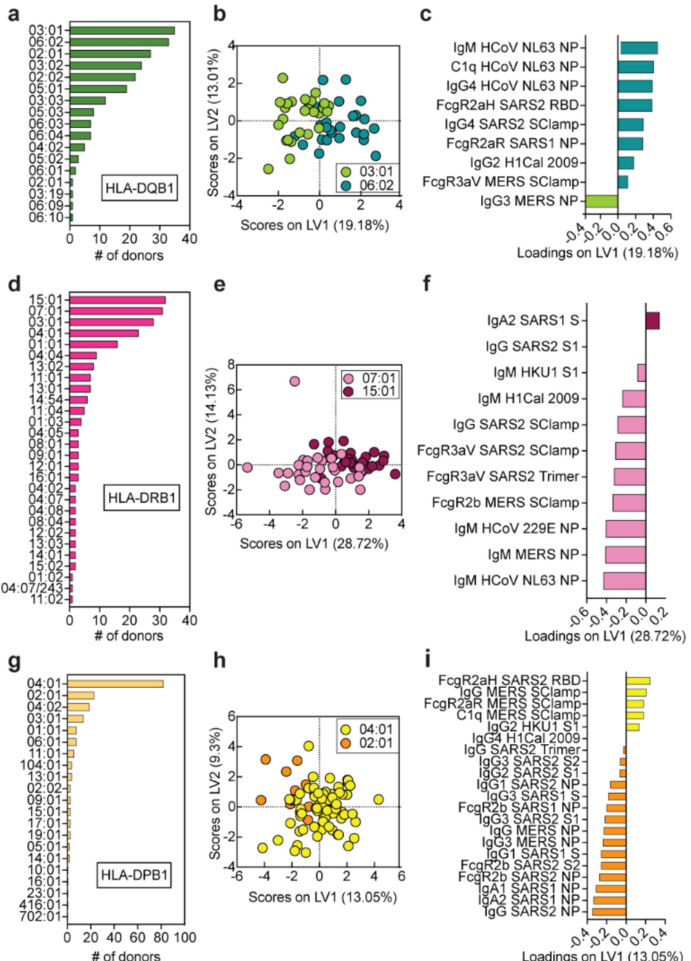


Figure 2 HLA class II alleles influence Ab signatures

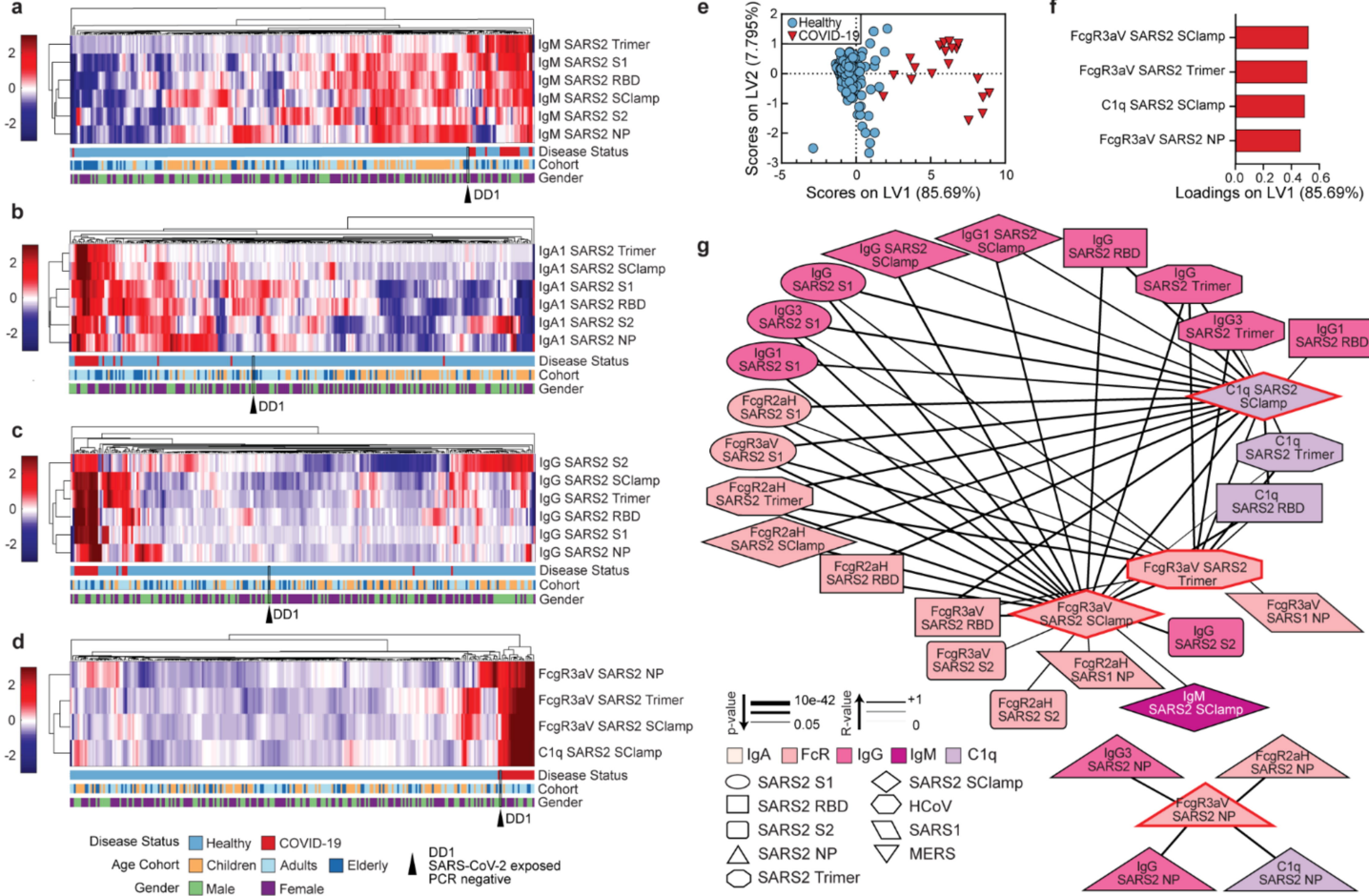


Figure 3 Healthy versus COVID-19 serological signatures

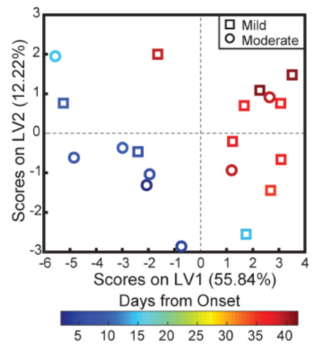
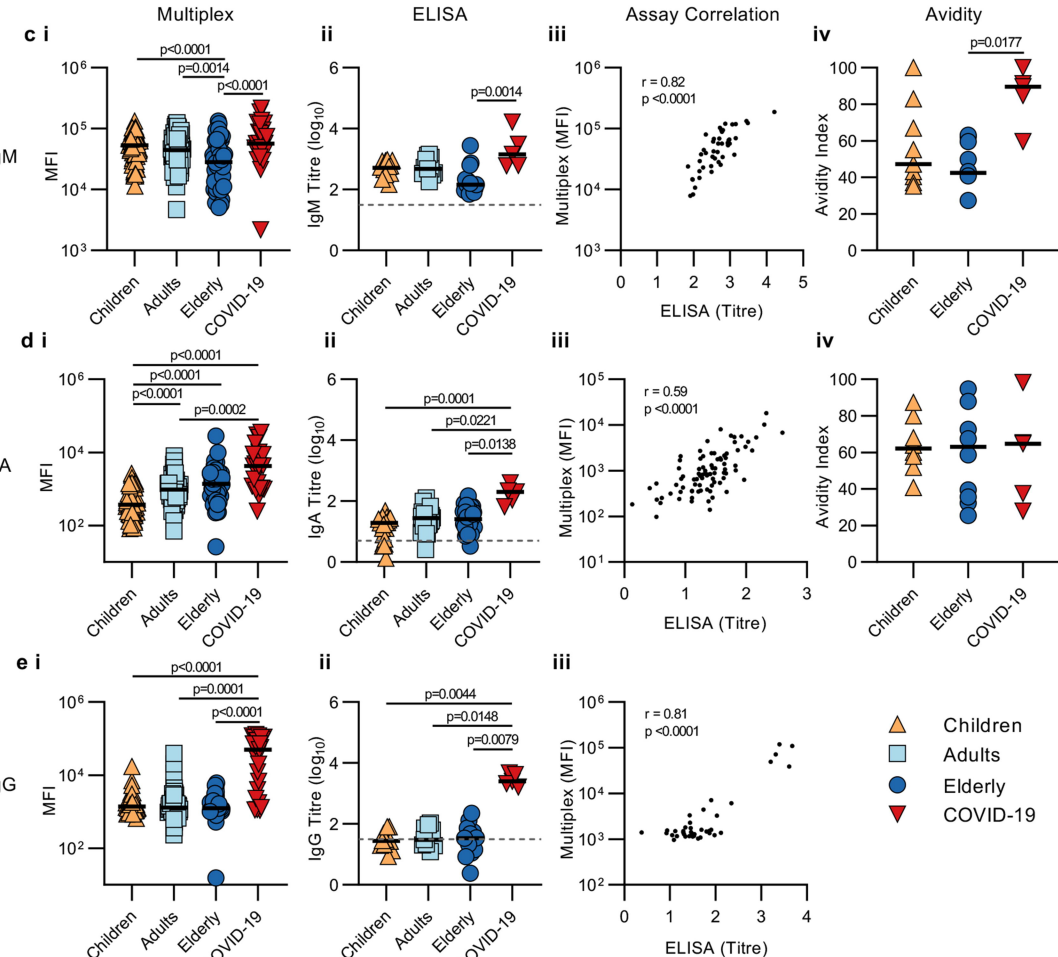
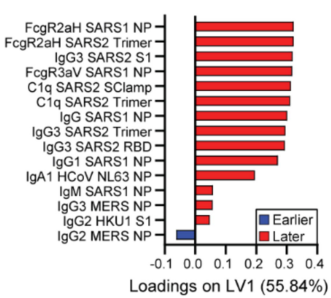
a**b**

Figure 4 COVID-19 Ab responses over time and Receptor Binding Domain Abs in healthy versus COVID-19